Spectroscopic and Computational Characterization of Substrate-Bound Mouse Cysteine Dioxygenase: Nature of the Ferrous and Ferric Cysteine Adducts and Mechanistic Implications[†]

Jessica D. Gardner,[‡] Brad S. Pierce,[§] Brian G. Fox,[‖] and Thomas C. Brunold*,[‡]

[‡]*Departments of Chemistry, and* [‖]*Biochemistry, University of Wisconsin—Madison, Madison, Wisconsin 53706, and* [§]*Department of Chemistry and Biochemistry, University of Texas, Arlington, Texas 76019*

ABSTRACT: Cysteine dioxygenase (CDO) is a mononuclear non-heme Fe-dependent dioxygenase that catalyzes the initial step of oxidative cysteine catabolism. Its active site consists of an Fe(II) ion ligated by three histidine residues from the protein, an interesting variation on the more common 2-His-1-carboxylate motif found in many other non-heme Fe(II)-dependent enzymes. Multiple structural and kinetic studies of CDO have been carried out recently, resulting in a variety of proposed catalytic mechanisms; however, many open questions remain regarding the structure/function relationships of this vital enzyme. In this study, resting and substrate-bound forms of CDO in the Fe(II) and Fe(III) states, both of which are proposed to have important roles in this enzyme's catalytic mechanism, were characterized by utilizing various spectroscopic methods. The nature of the substrate/active site interactions was also explored using the cysteine analogue selenocysteine (Sec). Our electronic absorption, magnetic circular dichroism, and resonance Raman data exhibit features characteristic of direct S (or Se) ligation to both the high-spin Fe(II) and Fe(III) active site ions. The resulting Cys- (or Sec-) bound species were modeled and further characterized using density functional theory computations to generate experimentally validated geometric and electronic structure descriptions. Collectively, our results yield a more complete description of several catalytically relevant species and provide support for a reaction mechanism similar to that established for many structurally related 2-His-1-carboxylate Fe(II)-dependent dioxygenases.

Cysteine dioxygenase (CDO)[1] is a non-heme Fe(II) dioxygenase that catalyzes the first step of oxidative cysteine catabolism, adding both O atoms from molecular oxygen to L-cysteine (Cys) to form cysteinesulfinic acid (*1, 2*). Cys, one of two sulfur-containing amino acids, is a necessary component in synthesizing new proteins and also serves as a precursor for several biologically important molecules, such as coenzyme A and glutathione (*3, 4*). Additionally, products of the CDO reaction are essential for the biosynthesis of pyruvate, taurine, and hypotaurine. Elevated Cys levels are known to have an excitotoxic effect resulting in neuronal damage and also have been implicated in a variety of neurological disorders, including Parkinson's, Alzheimer's, and motor neuron disease, and autoimmune disorders such as rheumatoid arthritis (*5–9*). Thus, CDO is a vital

enzyme both for providing important metabolites that are formed in subsequent reactions and for maintaining healthy Cys levels in the body.

The first crystal structure and subsequent X-ray absorption spectroscopic data appeared to indicate that the Fe of CDO is in a six-coordinate, distorted octahedral ligand environment consisting of three His residues and three solvent molecules. However, a more recent crystal structure revealed that the active site of CDO actually comprises an Fe(II) ion coordinated by three His residues and a single solvent molecule to complete a distorted tetrahedral coordination geometry (*10–12*). This 3-His facial metal-binding motif is similar to, but still noticeably different from, the more common 2-His-1-carboxylate motif observed at the active sites of several other Fe(II)-dependent oxygenases (*13–15*). Although uncommon, this 3-His metal-binding motif has also been observed in other enzymes. For example, diketone dioxygenase (Dke1), which catalyzes the O_2-dependent cleavage of C—C bonds of β-diketones like acetylacetone, contains an Fe(II) ion ligated by three His residues in an arrangement very similar to that seen in CDO (*14, 16*).

Another interesting feature of the CDO active site is that the thiol group of Cys93 is covalently linked to Tyr157, a posttranslational modification that is also observed in galactose oxidase (*17, 18*). Although Tyr157 is not a ligand to the metal in CDO, it is close enough to be involved in H-bonding interactions with coordinated solvent or with the cosubstrate O_2 during catalysis. However, it is still unclear exactly how the unique active site structure affects the function of this enzyme.

[1]Abbreviations: Abs, electronic absorption; ADF, Amsterdam density functional; BPS, bathophenanthrolinedisulfonic acid; CDO, cysteine dioxygenase; CT, charge transfer; DFT, density functional theory; Dke1, diketone cleaving enzyme; HEPES, 4-(2-hydroxyethyl)-1-piperazineethanesulfonic acid; IPTG, isopropyl β-D-1-thiogalactopyranoside; LT, low temperature; MBP, maltose binding protein; MCD, magnetic circular dichroism; MO, molecular orbital; PDB, Protein Data Bank; rR, resonance Raman; SDS—PAGE, sodium dodecyl sulfate—polyacrylamide gel electrophoresis; Sec, selenocysteine; SOR, superoxide reductase; TCEP, tris(2-carboxyethyl)phosphine; TEV, tobacco etch virus; TLC, thin-layer chromatography; VTVH, variable temperature, variable field; XAS, X-ray absorption spectroscopy.

The recent publication of X-ray crystal structures of resting and substrate-bound CDO led to a variety of proposed catalytic mechanisms for this enzyme, each highlighting different potential relationships between structure and function (*10−12, 19, 20*). However, many open questions remain concerning the nature of substrate binding within the active site of CDO and the details of subsequent steps of the catalytic cycle. In this work, the resting state and various substrate- (analogue-) bound forms of CDO have been studied using a combination of electronic absorption (Abs), magnetic circular dichroism (MCD), and resonance Raman (rR) spectroscopies, as well as density functional theory (DFT) computations. Results from these investigations provide unprecedented insight into the electronic structures of both the Fe(II)- and Fe(III)-bound states of CDO in the presence of substrate. These spectroscopic and computational results are discussed in relation to existing structural data for this enzyme, as well as to the proposed mechanistic schemes.

EXPERIMENTAL PROCEDURES

Protein Expression and Purification. CDO was expressed as a fusion to maltose binding protein (MBP) in *Escherichia coli* BL21(DE3)pLysS cells (Novagen). Cell growth and induction of gene expression using IPTG were performed as described previously (*21*). The harvested cell paste was resuspended in buffer (25 mM HEPES, 200 mM NaCl, pH 7.5), treated with lysozyme, DNase, and RNase for 30 min, and sonicated to disrupt the cells. This suspension was then centrifuged for 1 h at 20000 rpm at 4 °C. To isolate CDO, the resulting supernatant was loaded onto an amylose column, to which MBP binds. After the nonbinding proteins were washed from the column, CDO was cleaved from MBP on the column by incubating with tobacco etch virus (TEV) protease overnight at 4 °C. CDO was then washed from the column, concentrated, and loaded onto a Superdex 200 size-exclusion column to separate it from any remaining contaminants. Fractions containing CDO, identified using SDS−PAGE, were pooled and concentrated.

Enzyme Activity. Enzyme activity was determined qualitatively as follows. Reaction mixtures containing 10 μM CDO and 10 mM Cys (or Sec) in HEPES buffer (pH 7.5) or phosphate buffer (pH 7) were incubated at 37 °C for up to 90 min. Samples were removed for analysis at regular intervals, at which time the protein was heat-denatured (at 95 °C) to stop the reaction. The samples were then centrifuged for 5 min, and 1 μL of the supernatant was spotted onto a silica gel thin-layer chromatography (TLC) plate. Plates were run in a 20%:20%:60% (v/v) H_2O/acetic acid/1-butanol solution for 45 min and stained with a 1.5% (w/v) ninhydrin solution (3% (v/v) acetic acid in ethanol). Upon heat activation of the stain, bands associated with the reactants (Cys or Sec) and product (cysteinesulfinic acid) could readily be identified by using appropriate standards.

Sample Preparation. Approximate protein concentrations were determined spectrophotometrically using an ε_{280} value of 25300 M^{-1} cm^{-1}. Fe content was determined using a colorimetric assay with bathophenanthrolinedisulfonic acid (BPS) as described previously (*21*). Samples used for spectroscopy contained CDO with a final Fe concentration of ~1 mM in buffer consisting of 25 mM HEPES and 200 mM NaCl (pH 7.5). Fe(III)-CDO was reduced anaerobically to Fe(II)-CDO by adding sodium dithionite until a complete loss of color was observed and no further change to the Abs spectrum occurred. Samples containing substrate (analogue) were prepared anaerobically and contained

a 2-fold excess of cysteine or selenocysteine. Selenocysteine was prepared by anaerobic reduction of selenocystine with tris-(2-carboxyethyl)phosphine (TCEP). All samples used for low-temperature (LT) Abs and MCD experiments also contained 55% (v/v) glycerol.

Spectroscopy. Room temperature Abs spectra were obtained using a Varian Cary 5e spectrophotometer. The sample compartment was purged with $N_2(g)$ when collecting data for anaerobic samples. LT (4.5 K) Abs and MCD spectra were obtained using a Jasco J-715 spectropolarimeter in conjunction with an Oxford Instruments SM4000-8T magnetocryostat. The MCD spectra presented herein were obtained by subtracting the −7 T data from the +7 T data. Variable-temperature, variable-field (VTVH) MCD data were collected by measuring the MCD signal intensity as a function of applied magnetic field for several fixed temperatures at a constant wavelength. These data were analyzed quantitatively using a fitting program developed by Dr. Frank Neese (*22*).

Resonance Raman (rR) data were obtained by exciting the samples with 647.1 or 752.5 nm light from a Kr$^+$ ion laser (Coherent I-302C). The power of the incident light was ~25 mW. Light scattered at ~135° from the sample was dispersed by a triple monochromator (Acton Research SpectraPro) with a 1200 g/mm grating and detected with a liquid N_2-cooled back-illuminated CCD camera (Princeton Instruments Spec-10 100BR, 1340 × 100 pixels). The EPR tubes containing the samples were immersed in liquid N_2 during data collection.

Computations. Computational models of the Cys- or Sec-bound Fe-CDO active site were generated by spin-unrestricted density functional theory (DFT) geometry optimizations using the Amsterdam Density Functional (ADF) 2006.01 software package (*23−26*). The calculations employed ADF basis set IV (triple-ζ with single polarization), an integration constant of 4.0, the Vosko−Wilk−Nusair local density approximation (*27*), and the nonlocal gradient corrections of Becke (*28*) and Perdew (*29*). Core orbitals were frozen through 1s (O, N, C), 2p (Fe, S), or 3p (Se). Initial structures were derived from published X-ray crystallographic data for Cys-bound human Fe(II)-CDO (*12, 30*). The models included the three first-sphere His residues ligated to a high-spin Fe(II) or Fe(III) ion, as well as a bidentate Cys or Sec ligand. The His residues were modeled as 4-ethylimidazole with the terminal methyl groups held frozen during the optimization. The positions of all other atoms were allowed to vary. Spin-unrestricted single-point calculations were carried out on the optimized structures using the ADF 2008.01 software and the parameters listed above.

RESULTS

Although CDO is an Fe(II)-dependent enzyme, the as-isolated protein used for these studies actually contained substoichiometric amounts of Fe (~50% occupation). However, because the metal-free sites did not contribute to the spectra presented in this paper, no attempt was made to reconstitute the protein with additional Fe(II). Sample concentrations given herein refer to the concentration of Fe-bound CDO rather than total protein. Qualitative TLC activity assays were performed to verify that the CDO used in these studies was indeed active (data not shown).

Spectroscopic Data. (*A*) *Fe(II)-CDO.* As-isolated CDO is pale yellow in color, and a colorimetric assay using batho-phenanthrolinedisulfonate (BPS) revealed the presence of both
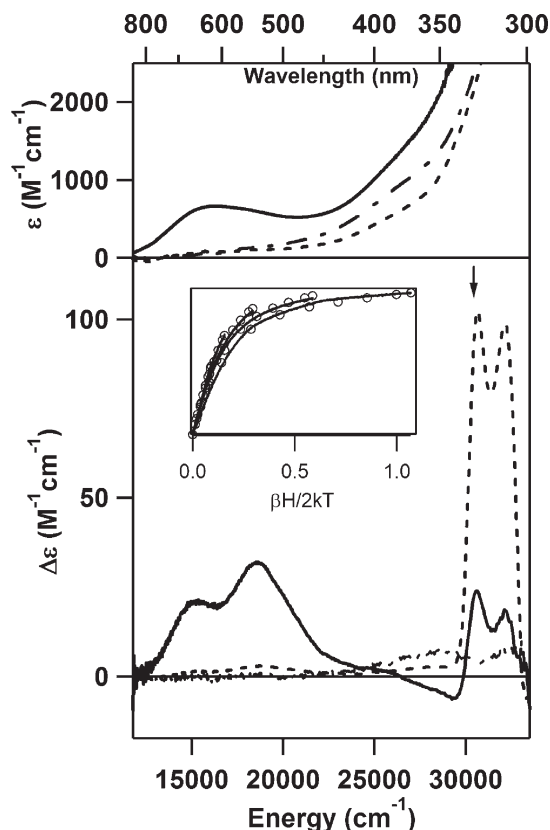
FIGURE 1: Room temperature Abs (top) and 4.5 K MCD (bottom) spectra of as-isolated CDO (− - −), Fe(II)-CDO + Cys (- - -), and as-isolated CDO + Cys (—). Inset: VTVH MCD data (—) collected for Fe(II)-CDO + Cys at 30580 cm^{-1} (position indicated by arrow) and 2.2, 4, 8, 15, and 25 K. Open circles represent a theoretical fit of the data obtained with the parameters $g = 2$, $S = 2$, $D = -13.0$ cm^{-1}, and $E/D = 0.23$.

Fe(II) (∼85% of the total Fe) and Fe(III) (remaining ∼15% of Fe) in this form of the enzyme. CDO becomes colorless upon the addition of dithionite, suggesting that the yellow color of the as-isolated enzyme is due to the Fe(III)-containing fraction. No distinguishing features are observed in the Abs or MCD spectra of the Fe(II)-CDO species (Figure 1).

Upon addition of Cys to Fe(II)-CDO, the solution remained colorless, and consequently no features are observed in the visible region of the corresponding Abs spectrum (Figure 1, top). However, reasonably intense temperature-dependent features are observed in the near-UV region of the MCD spectrum obtained for this species (Figure 1, bottom), which can be attributed to S(Cys) → Fe(II) charge transfer (CT) transitions on the basis of a comparison to data reported for enzymes with similar active site structures (*31*). The MCD saturation behavior of these features as a function of temperature and applied magnetic field is characteristic of a high spin ($S = 2$) Fe(II) species, as our VTVH MCD data could be fit well using the parameters $S = 2$, $D = -13.0$ cm^{-1}, and $E/D = 0.23$ (see Figure 1, inset). No discernible features are observed in the visible and near-IR regions of the MCD spectrum of Fe(II)-CDO complexed with Cys. After exposure to O$_2$, the observed MCD features decrease significantly in intensity, signifying enzymatic turnover of this Cys-bound Fe(II)-CDO species. This confirms that the Fe(II)-CDO fraction is the active form of the enzyme and suggests that the MCD features observed for this species prior to exposure to O$_2$ are due to a substrate-bound CDO species that participates in the catalytic cycle.
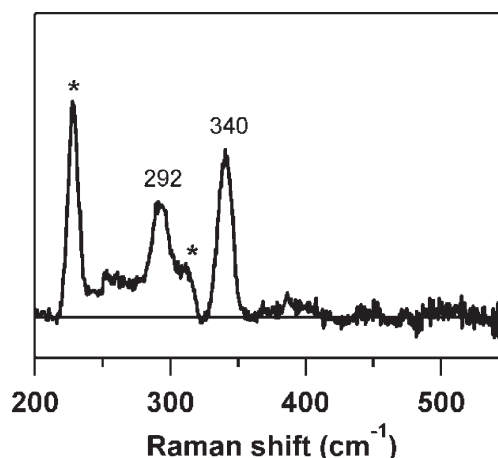

FIGURE 2: 77 K rR spectrum of as-isolated CDO + Cys, obtained with λ_{ex} = 647.1 nm. Features marked by an asterisk are due to vibrations of the ice lattice.

(*B*) *Fe(III)-CDO*. When as-isolated CDO is incubated with Cys, a change in color from pale yellow to blue is observed, indicating that Cys also binds to the minor (∼15% of the total Fe found by the BPS assay) fraction of Fe(III)-CDO. This Cys adduct of Fe(III)-CDO exhibits a dominant Abs feature at 15700 cm^{-1} (Figure 1, top) and temperature-dependent MCD features at 15250 and 18570 cm^{-1} (Figure 1, bottom). These Abs and MCD spectroscopic signatures of Cys-bound Fe(III)-CDO are remarkably similar to those displayed by Fe(III) superoxide reductase (*31*), a well-characterized non-heme Fe enzyme with a comparable active site structure (see below).

The rR spectrum of Cys-bound Fe(III)-CDO exhibits two distinct features at 340 and 292 cm^{-1} (Figure 2). These data are consistent with Cys ligation to Fe(III) and, on the basis of comparison to other known Fe(III)-Cys species, can be assigned as Fe−S stretching and S−C−C bending modes, respectively (*32*). Enhancement of these modes is observed only with excitation wavelengths near the dominant Abs band exhibited by Cys-bound Fe(III)-CDO, corroborating our assignment of this band as a S → Fe(III) CT transition.

Upon exposure of a sample containing Cys-bound Fe(III)-CDO to O$_2$, the blue color as well as the Abs, MCD, and rR features described above was preserved, signifying that this species is not directly involved in catalysis. Nevertheless, because Fe(III) intermediates are proposed to be involved in CDO's catalytic mechanism (*10, 12, 20*), characterization of this Cys-bound Fe(III)-CDO species as well as related species containing O$_2$ analogues can provide useful mechanistic insight.

(*C*) *Sec-Bound CDO*. Selenocysteine (Sec) is an interesting Cys analogue, differing from the latter only in the presence of Se instead of S in the amino acid side chain. Interestingly, however, the TLC-based activity assays indicated that CDO could not catalyze the oxidation of Sec (data not shown). Addition of Sec to as-isolated CDO demonstrates the ability of Sec to interact with the enzyme active site in a manner very similar to that seen with Cys. The Abs spectrum of Sec-bound CDO shows a dominant feature at 13250 cm^{-1} that is similar in appearance to that exhibited by Cys-bound CDO (Figure 3, top). Likewise, several features are observed in the MCD spectrum of Sec-bound CDO that are reminiscent of those displayed by Cys-bound CDO. By comparison to the spectra of the Cys-bound CDO species as well as from a comparison of the data for the as-isolated and fully reduced Sec-bound CDO species, the MCD features observed for
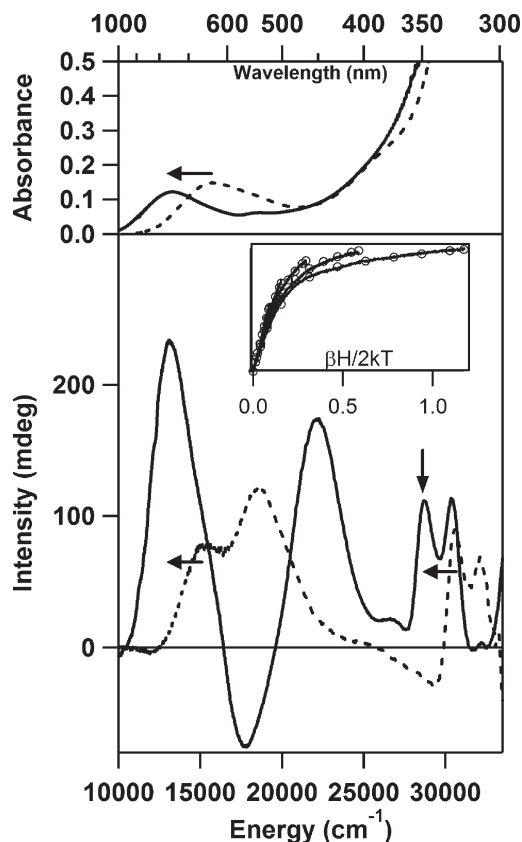
FIGURE 3: Room temperature Abs (top) and 4.5 K MCD (bottom) spectra of as-isolated CDO + Cys (- - -) or Sec (——). Horizontal arrows depict the marked red shifts of features upon substitution of Cys with Sec. Inset: VTVH MCD data (——) collected for Fe(II)-CDO + Sec at 28818 cm^{-1} (position indicated by vertical arrow) and 2, 4, 8, 15, and 25 K. Open circles represent a theoretical fit of the data obtained with the parameters $g = 2$, $S = 2$, $D = -9.0$ cm^{-1}, and $E/D = 0.25$.
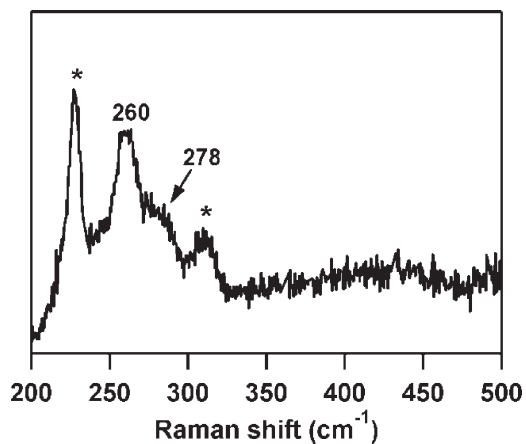

FIGURE 4: 77 K rR spectrum of as-isolated CDO + Sec, obtained with $\lambda_{ex} = 752.5$ nm. Features marked by an asterisk are due to vibrations of the ice lattice.

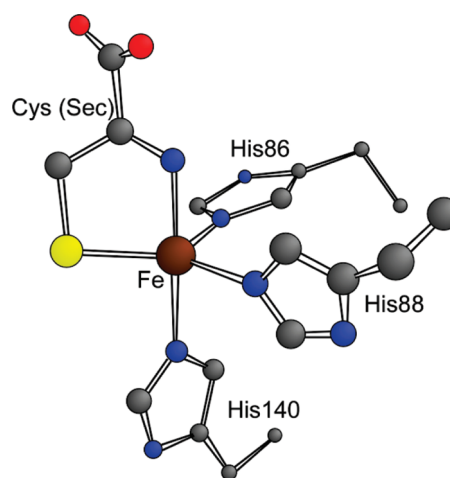FIGURE 5: DFT-optimized active site model of Cys- (or Sec-) bound Fe(III)-CDO. H atoms have been omitted for clarity.

Sec-bound CDO at lower energy are attributed to the Fe(III)-containing CDO fraction, and those at higher energy are attributed to the Fe(II)-containing fraction (Figure 3, bottom). These MCD features have greater intensity than those observed for Cys-bound CDO as a result of the increased spin−orbit coupling for Se compared to S. Like the dominant Abs band, the MCD features due to both the Fe(II)- and Fe(III)-CDO species complexed with Sec are noticeably red shifted compared to their counterparts in the spectra of Cys-bound CDO. Given that the first ionization potential of Se is lower than that of S, this red shift of the Se → Fe CT transitions relative to their S → Fe CT counterparts is to be expected. The origin of these red shifts is further explored below. VTVH MCD data were also collected for the Sec-bound Fe(II)-CDO species (see Figure 3, inset). As for the analogous Cys-bound species, our fit indicates that these data are characteristic of a high-spin ($S = 2$) Fe(II) species with a large, negative D value and high rhombicity ($D = -9.0$ cm^{-1}, $E/D = 0.25$) .

The rR spectrum of Sec-bound Fe(III)-CDO exhibits a distinct peak at 260 cm^{-1} with a small but noticeable shoulder at 278 cm^{-1} (Figure 4). Considering the large change in mass upon substitution of Se for S and the expectation that this mass difference will have a larger effect on the Fe−S stretching frequency than the S−C−C bending frequency, these observed peaks can be assigned as the ν(Fe−Se) stretching and δ(Se−C−C) bending modes, respectively. Enhancement of these vibrational modes upon

excitation near the dominant Abs band indicates that this band arises from a Se → Fe(III) CT transition, analogous to the S → Fe(III) CT transition of the Cys-bound Fe(III)-CDO species.

Computations. To gain a more complete understanding of the electronic properties of Cys- and Sec-bound CDO, active site models were generated from X-ray crystallographic coordinates of Cys-bound human Fe(II)-CDO (PDB code 2IC1) using DFT methods, and their geometric and electronic structures were analyzed. Four models were considered in this study, namely, Cys- and Sec-bound Fe(III)-CDO and Cys- and Sec-bound Fe(II)-CDO. Each model included the three coordinating His residues and the bidentate Cys or Sec substrate directly ligated to the central Fe ion (Figure 5). Table 1 compares key structural parameters derived from the DFT-optimized models and the X-ray crystal structure of Cys-bound Fe(II)-CDO. Overall, the geometric structures of the computational models are quite reasonable and in good agreement with the available crystal structure data. Each optimized model possesses a nearly trigonal bipyramidal active site structure with His86, His88, and the S of Cys (or Se of Sec) comprising the equatorial plane perpendicular to the axis defined by His140 and the N of Cys (or Sec). One noticeable feature of the Cys-bound Fe(II)-CDO model is that the optimized Fe−S distance is significantly longer than the experimentally determined distance; however, this calculated

Table 1: Structural Parameters for DFT-Optimized CDO Models Compared to Crystal Structure Data for Cys-Fe(II)-CDO[a]

	Fe−N$_{His86}$	Fe−N$_{His88}$	Fe−N$_{His140}$	Fe−N$_{Cys(Sec)}$	Fe−S(Se)
2IC1[b]	2.036	2.071	2.019	2.030	2.020
Cys-Fe(III)-CDO	2.099	2.171	2.176	2.163	2.274
Sec-Fe(III)-CDO	2.113	2.164	2.179	2.165	2.413
Cys-Fe(II)-CDO	2.140	2.193	2.222	2.177	2.257
Sec-Fe(II)-CDO	2.138	2.205	2.219	2.150	2.405

[a]All bond lengths are given in Å. [b]Reference *12*.

Table 2: Experimental and Calculated Transition Energies (in cm^{-1}) for Cys- and Sec-Bound Fe(II)- and Fe(III)-CDO Species

calcd	S(Se) p$_y$ → Fe d$_{xy}$	S(Se) p$_y$ → Fe d$_{x^2-y^2}$
Cys-Fe(III)-CDO	17002	21858
Sec-Fe(III)-CDO	15679	19962
Cys-Fe(II)-CDO	NA	NA
Sec-Fe(II)-CDO	NA	NA

exptl	Abs	MCD
Cys-Fe(III)-CDO	15700	15250, 18570
Sec-Fe(III)-CDO	13250	13100, 17750, 22100
Cys-Fe(II)-CDO	> 28000	30600, ~32100
Sec-Fe(II)-CDO	> 27000	28700, 30400

distance is quite comparable to Fe−S distances observed in crystal structures of other known complexes with similar Fe coordination spheres (*33, 34*). Interestingly, although the calculated Fe−N distances are slightly longer in the Fe(II) models than in their Fe(III) counterparts, as expected, the Fe−S and Fe−Se distances are shorter. A possible explanation for this somewhat counterintuitive finding is that because Fe(II) is a softer acid than Fe(III), it engages in a stronger bonding interaction with the soft S and Se ligand atoms.

To further validate these computational models, electronic transition energies were calculated and compared to those determined experimentally by Abs and MCD spectroscopies. These calculations were performed using the method of Slater, wherein 0.5 electron was transferred from the donor molecular orbital (MO) to the acceptor MO associated with the transition of interest. The transition energy was then calculated from the difference between these MO energies after SCF convergence had been reached. For each of the Fe(III)-CDO models, the Slater method was used to calculate the energies of the S/Se → Fe CT transitions arising from both the σ- and π-type S/Se-based MOs (see below). The results from these calculations are listed in Table 2 along with the experimental Abs and MCD transition energies. The good agreement between the calculated and experimental transition energies and the accurate reproduction of the red shifts upon substitution of Cys with Sec warrant a more detailed analysis of the electronic structures of these optimized models.

MO energies and compositions were calculated using spin-unrestricted DFT computations. For the Fe(III)-CDO models, the five unoccupied Fe(III) 3d-based spin-down MOs display a splitting pattern consistent with a trigonal bipyramidal geometry; namely, the d$_{xz}$- and d$_{yz}$-based MOs lie lowest in energy, followed by the d$_{xy}$- and d$_{x^2-y^2}$-based orbitals, while the d$_{z^2}$-based MO is highest in energy (Figure 6). Among the highest energy occupied ligand-based MOs are two S- or Se-based orbitals, with the one possessing σ-bonding character with respect to the S/Se−Fe bond being lower in energy than that having π-bonding character.
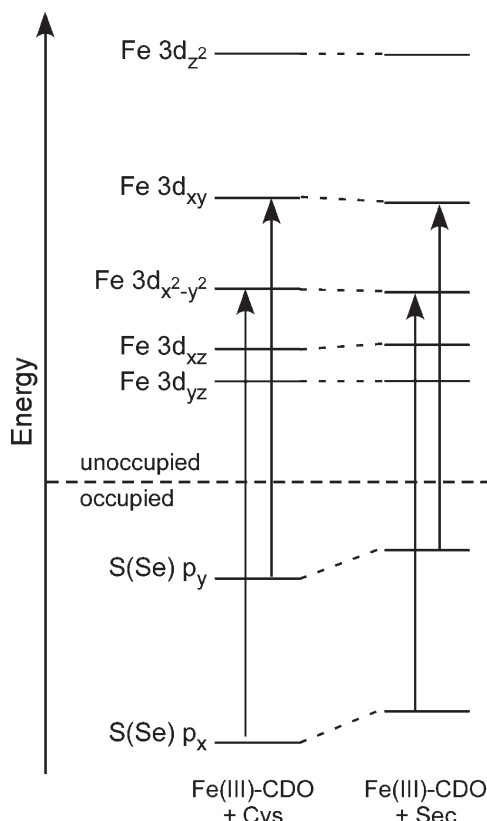

FIGURE 6: Relevant portions of the DFT-computed MO diagrams for Cys- and Sec-bound Fe(III)-CDO. Only the spin-down MOs are shown. The S(Se) → Fe CT transitions are indicated by arrows.

The DFT-computed compositions of the relevant occupied S- and Se-based MOs as well as the unoccupied Fe 3d-based spin-down MOs of the Cys- and Sec-bound Fe(III)-CDO models are presented in Table 3. Although compared to their Cys-based counterparts the frontier MOs of Sec are closer in energy to the Fe 3d orbitals (Figure 6) and thus could engage in stronger metal−ligand bonding interactions, the Fe−Se bond is significantly longer than the Fe−S bond, effectively reducing the degree of overlap between the Se and Fe orbitals. As a result, the Fe−S and Fe−Se bonds in these substrate-bound Fe(III)-CDO computational models display very similar degrees of covalency.

The same basic trends are observed for the Fe(II)-CDO models; that is, the two highest energy occupied Se-based MOs of the Sec-bound Fe(II)-CDO model are predicted to be at a higher energy than their S-based counterparts in the Cys-bound Fe(II)-CDO model (Figure 7). As was observed for the Fe(III)-CDO models, however, this difference in relative energies of the Cys and Sec frontier MOs causes only minor differences in the computed Fe−S and Fe−Se bond covalencies of the substrate-bound Fe(II)-CDO models (Table 4).

DISCUSSION

Although CDO was discovered and initially studied over 40 years ago, much of the current knowledge of this vital enzyme has been gained very recently (*2, 35, 36*). Following several structural studies and standard biochemical characterization, many different reaction mechanisms were proposed (*10−12, 19−21, 37*). However, the lack of an in-depth understanding of the electronic structure of CDO has thus far prevented a critical evaluation of the numerous viable mechanisms. To address this issue, we have

Table 3: DFT-Computed Compositions (%) of the Occupied S- and Se-Based and Unoccupied Fe 3d-Based Spin-Down MOs for the Optimized Cys- and Sec-Bound Fe(III)-CDO Active Site Models

MO[a]	occ[b]	Fe 3d orbitals					S, Se	
		z^2	xy	$x^2 - y^2$	xz	yz	p_y	p_x
Fe(III)-CDO + Cys								
Fe $3d_{z^2}$	0	70	0	0	0	0	0	8
Fe $3d_{xy}$	0	2	43	23	0	0	15	2
Fe $3d_{x^2-y^2}$	0	0	23	47	0	0	8	8
Fe $3d_{xz}$	0	0	0	0	88	0	1	0
Fe $3d_{yz}$	0	0	0	0	0	50	0	0
S p_y	1	0	16	0	0	0	45	0
S p_x	1	3	0	9	1	0	0	30
Fe(III)-CDO + Sec								
Fe $3d_{z^2}$	0	71	0	0	0	0	0	8
Fe $3d_{xy}$	0	1	42	25	0	0	15	2
Fe $3d_{x^2-y^2}$	0	0	24	45	1	0	9	9
Fe $3d_{xz}$	0	0	0	0	88	0	1	0
Fe $3d_{yz}$	0	0	0	0	0	49	1	0
Se p_y	1	0	18	0	0	0	53	0
Se p_x	1	5	0	11	0	0	0	47

[a]Dominant orbital contributor. [b]MO occupancies.

Table 4: DFT-Computed Compositions (%) of the Relevant Spin-Down MOs for the Optimized Cys- and Sec-Bound Fe(II)-CDO Active Site Models

| MO[a]	occ[b]	Fe 3d orbitals					S, Se	
		z^2	xy	$x^2 - y^2$	xz	yz	p_y	p_x
Fe(II)-CDO + Cys								
Fe $3d_{z^2}$	0	21	0	8	0	0	0	4
Fe $3d_{xy}$	0	5	59	7	0	0	15	0
Fe $3d_{x^2-y^2}$	0	6	13	54	0	0	2	4
Fe $3d_{yz}$	0	0	0	0	1	81	0	0
Fe $3d_{xz}$	1	0	0	0	82	1	0	0
S p_y	1	0	14	0	0	0	68	0
S p_x	1	3	0	10	1	0	0	61
Fe(II)-CDO + Sec								
Fe $3d_{z^2}$	0	19	0	7	0	0	0	4
Fe $3d_{xy}$	0	6	53	12	0	3	12	0
Fe $3d_{x^2-y^2}$	0	5	19	48	3	0	4	3
Fe $3d_{yz}$	0	0	0	2	0	80	0	0
Fe $3d_{xz}$	1	0	2	1	83	0	0	0
Se p_y	1	0	13	0	0	0	66	0
Se p_x	1	4	0	10	0	0	0	67

[a]Dominant orbital contributor. [b]MO occupancies.
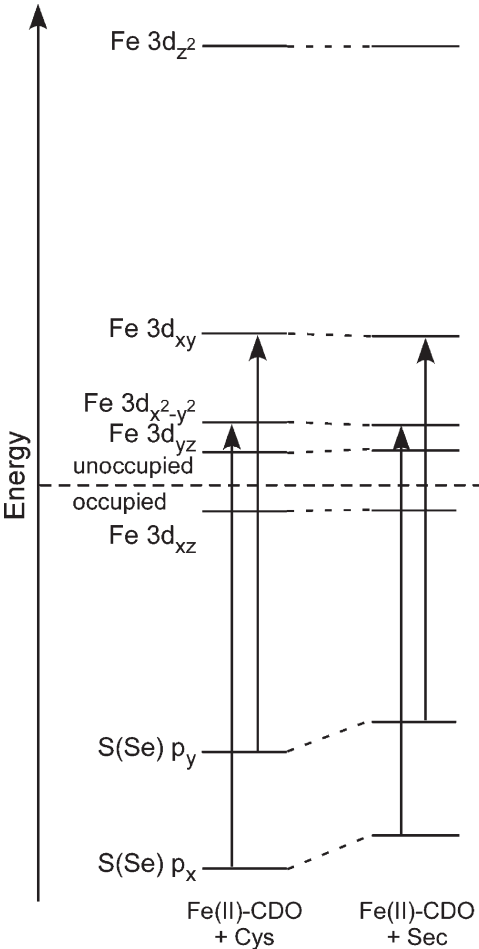
FIGURE 7: Relevant portions of the DFT-computed MO diagrams for Cys- and Sec-bound Fe(II)-CDO. Only the spin-down MOs are shown. The S(Se) → Fe CT transitions are indicated by arrows.

the geometric and electronic structures of various substrate-(analogue-) bound forms of CDO.

Previous studies revealed that CDO can bind different metal ions but is active only with Fe(II) within its active site (*10*, *38*, *39*). The ability to characterize resting Fe(II)-CDO spectroscopically is somewhat limited because this form of the protein is colorless, with no distinguishing features discernible by either Abs or MCD spectroscopies, even in the near-IR region. Previous studies by Solomon and co-workers revealed that the near-IR region of the MCD spectra of Fe(II)-containing proteins and synthetic complexes provides insight into the metal ion coordination number (*40*). Specifically, features arising from ligand-field transitions are observed near 10000 cm^{-1} for both five- and six-coordinate Fe(II) species, but only at significantly lower energy ($\sim$4000−7000 cm^{-1}) for four-coordinate Fe(II) species. Thus, because the MCD spectrum of Fe(II)-CDO lacks any discernible features near 10000 cm^{-1}, our data are more consistent with the generally accepted four-coordinate, distorted tetrahedral CDO resting state. However, considering that the near-IR MCD features of similar Fe(II) species are weak and, even in the case of five- or six-coordinate species, would be expected to appear near the wavelength limit of our instrument (*40*), the possibility of a six-coordinate, distorted octahedral resting state cannot be ruled out definitively on the basis of our data.

Although resting Fe(II)-CDO has proven difficult to study spectroscopically, anaerobic addition of substrate Cys generates a species that is more amenable to spectroscopic characterization. Specifically, intense temperature-dependent features are observed around 30000 cm^{-1} in the MCD spectrum of this species (Figure 1, bottom), indicative of S-ligation to a high-spin Fe(II) ion. Exposure of this species to air, allowing enzymatic turnover to occur without replenishing the substrate, effectively eliminates these features from subsequent MCD spectra (Figure 8), confirming that the observed MCD features are associated with a substrate-bound form of CDO that is reactive toward O$_2$. On the basis of one X-ray crystal structure and XAS data, catalytic mechanisms were proposed involving no direct, or only a weak,

used a combination of several spectroscopic and computational techniques to develop experimentally validated descriptions of
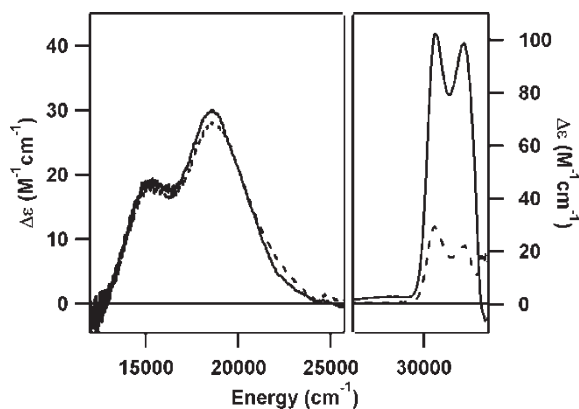
FIGURE 8: 4.5 K MCD spectra of as-isolated (left) and reduced (right) CDO + Cys before (—) and after (- - -) exposure to O_2.

interaction between the thiol group of Cys and the Fe(II) ion (*11*, *41*). However, in a more recent X-ray crystal structure of human CDO, Cys is clearly observed to coordinate directly to the Fe ion as a bidentate ligand (*12*). Additionally, another recent structure of rat CDO appears to contain a persulfenate moiety, demonstrating a possible reaction between Cys and O_2, both of which are coordinated directly to the active site Fe ion (*20*). Thus, some researchers have proposed mechanisms in which coordination of Cys via its thiol group to Fe is of fundamental importance (*10*, *12*, *20*, *21*). Our evidence for direct Cys ligation and the formation of a reasonably strong Fe−S bond under catalytically relevant conditions clearly favors this latter type of mechanistic proposal.

Our as-isolated enzyme also contains a sizable (~15%) fraction of Fe(III) within its active site. Very little was known about this Fe(III)-bound form of CDO prior to this study. Importantly, because the Abs, MCD, and rR spectral signatures are preserved when Cys-bound Fe(III)-CDO is exposed to O_2 (Figure 8), it can be concluded that this species is unable to catalyze the oxidation of cysteine to cysteinesulfinic acid. Nonetheless, a detailed characterization of Cys-bound Fe(III)-CDO is clearly warranted, as an Fe(III)-CDO species has been proposed to play a role in formation of the Cys-Tyr adduct near the active site (*42*). Additionally, many of the proposed catalytic mechanisms for CDO invoke the formation of Cys-bound Fe(III) species following the binding of cosubstrate O_2 to the active site (*10*, *12*, *20*). Studies of Cys-bound Fe(III)-CDO thus establish a suitable framework for future studies aimed at examining the properties of putative Fe(III)-superoxo species and at exploring O_2 (analogue) binding to the CDO active site. Therefore, we have also carried out spectroscopic and computational studies of both Cys- and Sec-bound Fe(III)-CDO species.

Our results indicate that Cys binds directly to a high-spin Fe(III) ion via its S atom in a manner similar to that observed for the active Fe(II)-bound form of CDO. This similar coordination is evidenced by the remarkable similarity between the S → Fe CT bands observed in the MCD spectra, the most noticeable difference being the dramatically red-shifted transitions for the Fe(III) species due to the greater ease of transferring electron density to the oxidized metal center. This similarity in the coordination of Cys to Fe(II)- and Fe(III)-CDO is reproduced nicely by our computational results, where both are described as five-coordinate, distorted trigonal bipyramidal species. This coordination environment leaves a large gap between the S(Cys) and His88 ligands (see Figure 5), providing adequate space for the binding and ideal positioning of cosubstrate O_2 for subsequent

reaction with the S atom of Cys. As such, CDO appears to employ the same basic strategy for substrate oxidation as that established for many structurally related 2-His-1-carboxylate Fe(II) dioxygenases (*13*, *15*, *43*).

Additional insights into the nature of the substrate/active site interactions were gained by using the Cys analogue Sec. The Abs, MCD, and rR spectra of both Cys- and Sec-bound CDO are quite similar, with the major differences being due to substitution of Se for S rather than a significant change in the substrate (analogue) binding mode (see Figures 2−4). Furthermore, the spectroscopic signatures of these species could be described quite effectively with nearly identical computational models. Our computational data suggest that the red shifts of the Abs and MCD spectral features of substrate-bound Fe(II)-CDO that are observed when Cys is substituted by Sec (see Figure 3) can be attributed to a destabilization of the Se-based MOs relative to their S-based counterparts and the consequent lowering of the corresponding CT transition energies. Collectively, these results also demonstrate that both Cys and Sec interact with the active site of CDO in a very similar manner. Intriguingly, however, despite the many similarities between Cys- and Sec-bound CDO, Sec does not appear to be a viable substrate for CDO.

Comparison to SOR. Superoxide reductase (SOR) is an Fe-dependent enzyme that catalyzes the reduction of the superoxide radical ($O_2 \cdot^-$) to H_2O_2 in anaerobic organisms. Its active site consisting of an Fe ion with predominantly N- and S-donor ligands (four equatorial His residues and an axial Cys residue in Fe(II)-SOR and an additional axial Glu residue in Fe(III)-SOR) is quite comparable to that of Cys-bound human CDO observed by X-ray crystallography and modeled computationally as described above (*12*, *33*). Extensive characterizations of SOR by structural, spectroscopic, and computational tools afforded a detailed understanding of the geometric and electronic structures of this enzyme (*31*, *32*). Key insights gained in these studies of SOR are briefly summarized below because they provide a valuable reference for a comparison with our results obtained for CDO.

The Abs spectrum of Fe(III)-SOR exhibits a dominant feature at 15150 cm^{-1} that was attributed to a S → Fe(III) CT transition (*31*). In the MCD spectrum related features are observed at 15150 and 18980 cm^{-1}, which were assigned as S → Fe(III) CT transitions originating from the S(Cys) p-based MOs possessing Fe−S π-bonding and σ-bonding character, respectively. Similar features, albeit at higher energy, are observed in the MCD spectrum of Fe(II)-SOR; because of their similarity to those exhibited by the Fe(III) species and consistent with subsequent analyses, these features were attributed to S → Fe(II) CT transitions. The remarkable similarity of the Abs and MCD spectra of Cys-bound CDO to those of SOR suggests that these species possess very similar Fe coordination environments, both in the Fe(II)- and in the Fe(III)-bound states.

The rR spectrum of Fe(III)-SOR obtained upon laser excitation into the dominant Abs band exhibits numerous vibrational features in the low-frequency region (*32*). The large number of resonance-enhanced peaks was rationalized in terms of extensive kinematic coupling between the Fe−S stretching motion and several internal Cys vibrational motions. The modes with predominantly Fe−S stretching and S−C_β−C_α bending character were assigned to the features at 323 and 298 cm^{-1}, respectively. In the rR spectrum of CDO, analogous peaks are observed at 340 and 292 cm^{-1} that are therefore assigned to these same vibrational modes. The observation of only two resonance-enhanced

features in the rR spectrum of CDO suggests that kinematic coupling is less pronounced in this species. This observation is consistent with the structure of Cys-bound Fe(II)-CDO, where the nonplanarity of the Cys moiety would decrease the effectiveness of such coupling (*44, 45*). The higher frequency of the Fe−S stretching motion could reflect the lower coordination number of the Fe(III) ion in CDO (five-coordinate species) relative to SOR (six-coordinate). Fewer ligands around the Fe(III) ion in CDO would result in less overall donation of electron density to the metal, thus allowing for a stronger Fe−S bonding interaction. This conclusion is corroborated by a comparison to heme proteins, where a similar upshift of the Fe−S stretching frequency is observed from six- to five-coordinate heme species (*46−48*).

REFERENCES

1. Yamaguchi, K., and Hosokawa, Y. (1987) Cysteine dioxygenase. *Methods Enzymol. 143*, 395–403.
2. Lombardini, J. B., Singer, T. P., and Boyer, P. D. (1969) Cysteine oxygenase. II. Studies on the mechanism of the reaction with ^{18}oxygen. *J. Biol. Chem. 244*, 1172–1175.
3. Cooper, A. J. L. (1983) Biochemistry of sulfur-containing amino acids. *Annu. Rev. Biochem. 52*, 187–222.
4. Stipanuk, M. H. (2004) Sulfur amino acid metabolism: pathways for production and removal of homocysteine and cysteine. *Annu. Rev. Nutr. 24*, 539–577.
5. Heafield, M. T., Fearn, S., Steventon, G. B., Waring, R. H., Williams, A. C., and Sturman, S. G. (1990) Plasma cysteine and sulphate levels in patients with motor neurone, Parkinson's and Alzheimer's disease. *Neurosci. Lett. 110*, 216–220.
6. Pean, A. R., Parsons, R. B., Waring, R. H., Williams, A. C., and Ramsden, D. B. (1995) Toxicity of sulphur-containing compounds to neuronal cell lines. *J. Neurol. Sci. 129*, 107–108.
7. Slivka, A., and Cohen, G. (1993) Brain ischemia markedly elevates levels of the neurotoxic amino acid, cysteine. *Brain Res. 608*, 33–37.
8. Emery, P., Bradley, H., Gough, A., Arthur, V., Jubb, R., and Waring, R. H. (1992) Increased prevalence of poor sulphoxidation in patients with rheumatoid arthritis: effect of changes in the acute phase response and second line drug treatment. *Ann. Rheum. Dis. 51*, 318–320.
9. Gordon, C., Bradley, H., Waring, R. H., and Emery, P. (1992) Abnormal sulphur oxidation in systemic lupus erythematosus. *Lancet 339*, 25–26.
10. McCoy, J. G., Bailey, L. J., Bitto, E., Bingman, C. A., Aceti, D. J., Fox, B. G., and Phillips, G. N., Jr. (2006) Structure and mechanism of mouse cysteine dioxygenase. *Proc. Natl. Acad. Sci. U.S.A. 103*, 3084–3089.
11. Simmons, C. R., Liu, Q., Huang, Q., Hao, Q., Begley, T. P., Karplus, P. A., and Stipanuk, M. H. (2006) Crystal structure of mammalian cysteine dioxygenase. A novel mononuclear iron center for cysteine thiol oxidation. *J. Biol. Chem. 281*, 18723–18733.
12. Ye, S., Wu, X. A., Wei, L., Tang, D., Sun, P., Bartlam, M., and Rao, Z. (2007) An insight into the mechanism of human cysteine dioxygenase. Key roles of the thioether-bonded tyrosine-cysteine cofactor. *J. Biol. Chem. 282*, 3391–3402.
13. Koehntop, K. D., Emerson, J. P., and Que, L., Jr. (2005) The 2-His-1-carboxylate facial triad: a versatile platform for dioxygen activation by mononuclear non-heme iron(II) enzymes. *J. Biol. Inorg. Chem. 10*, 87–93.
14. Straganz, G. D., and Nidetzky, B. (2006) Variations of the 2-His-1-carboxylate theme in mononuclear non-heme Fe^{II} oxygenases. *ChemBioChem 7*, 1536–1548.
15. Leitgeb, S., and Nidetzky, B. (2008) Structural and functional comparison of 2-His-1-carboxylate and 3-His metallocentres in non-haem iron(II)-dependent enzymes. *Biochem. Soc. Trans. 36*, 1180–1186.
16. Straganz, G. D., Glieder, A., Brecker, L., Ribbons, D. W., and Steiner, W. (2003) Acetylacetone-cleaving enzyme Dke1: a novel C-C-bond-cleaving enzyme from *Acinetobacter johnsonii*. *Biochem. J. 369*, 573–581.
17. Ito, N., Phillips, S. E. V., Stevens, C., Ogel, Z. B., McPherson, M. J., Keen, J. N., Yadav, K. D. S., and Knowles, P. F. (1991) Novel thioether bond revealed by a 1.7 Å crystal structure of galactose oxidase. *Nature 350*, 87–90.
18. Whittaker, M. M., and Whittaker, J. W. (2003) Cu(I)-dependent biogenesis of the galactose oxidase redox cofactor. *J. Biol. Chem. 278*, 22090–22101.
19. Joseph, C. A., and Maroney, M. J. (2007) Cysteine dioxygenase: structure and mechanism. *Chem. Commun.*, 3338–3349.
20. Simmons, C. R., Krishnamoorthy, K., Granett, S. L., Schuller, D. J., Dominy, J. E., Jr., Begley, T. P., Stipanuk, M. H., and Karplus, P. A. (2008) A putative Fe^{2+}-bound persulfenate intermediate in cysteine dioxygenase. *Biochemistry 47*, 11390–11392.
21. Pierce, B. S., Gardner, J. D., Bailey, L. J., Brunold, T. C., and Fox, B. G. (2007) Characterization of the nitrosyl adduct of substrate-bound mouse cysteine dioxygenase by electron paramagnetic resonance: electronic structure of the active site and mechanistic implications. *Biochemistry 46*, 8569–8578.
22. Neese, F., and Solomon, E. I. (1999) MCD *C*-term signs, saturation behavior, and determination of band polarizations in randomly oriented systems with spin $S \geq 1/2$. Applications to $S = 1/2$ and $S = 5/2$. *Inorg. Chem. 38*, 1847–1865.
23. Baerends, E. J., Ellis, D. E., and Ros, P. (1973) Self-consistent molecular Hartree-Fock-Slater calculations: I. The computational procedure. *Chem. Phys. 2*, 41–51.
24. Fonseca Guerra, C., Snijders, J. G., te Velde, G., and Baerends, E. J. (1998) Towards an order-*n* DFT method. *Theor. Chem. Acc. 99*, 391–403.
25. Te Velde, G., and Baerends, E. J. (1992) Numerical integration for polyatomic systems. *J. Comput. Phys. 99*, 84–98.
26. Versluis, L., and Ziegler, T. (1988) The determination of molecular structures by density functional theory. The evaluation of analytical energy gradients by numerical integration. *J. Chem. Phys. 88*, 322–328.
27. Vosko, S. H., Wilk, L., and Nusair, M. (1980) Accurate spin-dependent electron liquid correlation energies for local spin density calculations: a critical analysis. *Can. J. Phys. 58*, 1200–1211.
28. Becke, A. D. (1986) Density functional calculations of molecular bond energies. *J. Chem. Phys. 84*, 4524–4529.
29. Perdew, J. P. (1986) Density-functional approximation for the correlation energy of the inhomogeneous electron gas. *Phys. Rev. B 33*, 8822–8824.
30. Berman, H. M., Westbrook, J., Feng, Z., Gilliland, G., Bhat, T. N., Weissig, H., Shindyalov, I. N., and Bourne, P. E. (2000) The protein data bank. *Nucleic Acids Res. 28*, 235–242.
31. Clay, M. D., Jenney, F. E., Hagedoorn, P. L., George, G. N., Adams, M. W. W., and Johnson, M. K. (2002) Spectroscopic studies of *Pyrococcus furiosus* superoxide reductase: implications for active-site structures and the catalytic mechanism. *J. Am. Chem. Soc. 124*, 788–805.
32. Clay, M. D., Jenney, F. E., Noh, H. J., Hagedoorn, P. L., Adams, M. W. W., and Johnson, M. K. (2002) Resonance Raman characterization of the mononuclear iron active-site vibrations and putative electron transport pathways in *Pyrococcus furiosus* superoxide reductase. *Biochemistry 41*, 9833–9841.
33. Yeh, A. P., Hu, Y., Jenney, F. E., Adams, M. W. W., and Rees, D. C. (2000) Structures of the superoxide reductase from *Pyrococcus furiosus* in the oxidized and reduced states. *Biochemistry 39*, 2499–2508.
34. Santos-Silva, T., Trincão, J., Carvalho, A. L., Bonifácio, C., Auchère, F., Raleiras, P., Moura, I., Moura, J. J. G., and Romão, M. J. (2006) The first crystal structure of class III superoxide reductase from *Treponema pallidum*. *J. Biol. Inorg. Chem. 11*, 548–558.
35. Sörbo, B., and Ewetz, L. (1965) The enzymatic oxidation of cysteine to cysteinesulfinate in rat liver. *Biochem. Biophys. Res. Commun. 18*, 359–363.
36. Ewetz, L., and Sörbo, B. (1966) Characteristics of the cysteinesulfinate-forming enzyme system in rat liver. *Biochim. Biophys. Acta 128*, 296–305.
37. de Visser, S. P. (2009) Elucidating enzyme mechanism and intrinsic chemical properties of short-lived intermediates in the catalytic cycles of cysteine dioxygenase and taurine/α-ketoglutarate dioxygenase. *Coord. Chem. Rev. 253*, 754–768.
38. Chai, S. C., Jerkins, A. A., Banik, J. J., Shalev, I., Pinkham, J. L., Uden, P. C., and Maroney, M. J. (2005) Heterologous expression, purification, and characterization of recombinant rat cysteine dioxygenase. *J. Biol. Chem. 280*, 9865–9869.
39. Simmons, C. R., Hirschberger, L. L., Machi, M. S., and Stipanuk, M. H. (2006) Expression, purification, and kinetic characterization of recombinant rat cysteine dioxygenase, a non-heme metalloenzyme necessary for regulation of cellular cysteine levels. *Protein Expression Purif. 47*, 74–81.
40. Solomon, E. I., Pavel, E. G., Loeb, K. E., and Campochiaro, C. (1995) Magnetic circular dichroism spectroscopy as a probe of the geometric and electronic structure of non-heme ferrous enzymes. *Coord. Chem. Rev. 144*, 369–460.

41. Chai, S. C., Bruyere, J. R., and Maroney, M. J. (2006) Probes of the catalytic site of cysteine dioxygenase. *J. Biol. Chem. 281*, 15774–15779.

42. Dominy, J. E., Jr., Hwang, J., Guo, S., Hirschberger, L. L., Zhang, S., and Stipanuk, M. H. (2008) Synthesis of amino acid cofactor in cysteine dioxygenase is regulated by substrate and represents a novel post-translational regulation of activity. *J. Biol. Chem. 283*, 12188–12201.

43. Ryle, M. J., and Hausinger, R. P. (2002) Non-heme iron oxygenases. *Curr. Opin. Chem. Biol. 6*, 193–201.

44. Han, S., Czernuszewicz, R. S., and Spiro, T. G. (1989) Vibrational spectra and normal mode analysis for [2Fe-2S] protein analogues using ^{34}S, ^{54}Fe, and ^{2}H substitution: coupling of Fe-S stretching and S-C-C bending modes. *J. Am. Chem. Soc. 111*, 3496–3504.

45. Han, J., Adman, E. T., Beppu, T., Codd, R., Freeman, H. C., Huq, L., Loehr, T. M., and Sanders-Loehr, J. (1991) Resonance Raman spectra of plastocyanin and pseudoazurin: evidence for conserved cysteine ligand conformations in cupredoxins (blue copper proteins). *Biochemistry 30*, 10904–10913.

46. Green, E. L., Taoka, S., Banerjee, R., and Loehr, T. M. (2001) Resonance Raman characterization of the heme cofactor in cystathionine β-synthase. Identification of the Fe-S(Cys) vibration in the six-coordinate low-spin heme. *Biochemistry 40*, 459–463.

47. Champion, P. M., Stallard, B. R., Wagner, G. C., and Gunsalus, I. C. (1982) Resonance Raman detection of an Fe-S bond in cytochrome P450$_{cam}$. *J. Am. Chem. Soc. 104*, 5469–5472.

48. Bangcharoenpaurpong, O., Champion, P. M., Hall, K. S., and Hager, L. P. (1986) Resonance Raman studies of isotopically labeled chloroperoxidase. *Biochemistry 25*, 2374–2378.